ELSEVIER

Dynamics of water droplets detached from porous surfaces of relevance to PEM fuel cells

A. Theodorakakos [b], T. Ous [a], M. Gavaises [a,*], J.M. Nouri [a], N. Nikolopoulos [b], H. Yanagihara [c]

[a] *School of Engineering and Mathematical Sciences, The City University, London, UK*
[b] *Fluid Research Co., Athens, Greece*
[c] *Toyota Motor Company Europe, Brussels, Belgium*

Abstract

The detachment of liquid droplets from porous material surfaces used with proton exchange membrane (PEM) fuel cells under the influence of a cross-flowing air is investigated computationally and experimentally. CCD images taken on a purpose-built transparent fuel cell have revealed that the water produced within the PEM is forming droplets on the surface of the gas-diffusion layer. These droplets are swept away if the velocity of the flowing air is above a critical value for a given droplet size. Static and dynamic contact angle measurements for three different carbon gas-diffusion layer materials obtained inside a transparent air-channel test model have been used as input to the numerical model; the latter is based on a Navier–Stokes equations flow solver incorporating the volume of fluid (VOF) two-phase flow methodology. Variable contact angle values around the gas–liquid–solid contact-line as well as their dynamic change during the droplet shape deformation process, have allowed estimation of the adhesion force between the liquid droplet and the solid surface and successful prediction of the separation line at which droplets loose their contact from the solid surface under the influence of the air stream flowing around them. Parametric studies highlight the relevant importance of various factors affecting the detachment of the liquid droplets from the solid surface.
© 2006 Elsevier Inc. All rights reserved.

Keywords: Water droplet detachment; Carbon gas-diffusion layer; Fuel cell; Modelling

1. Introduction

Over the last few years extensive research is performed by major automotive manufacturers in developing fuel cell systems as alternative power sources to the conventional internal combustion engines. Those systems may consume either gaseous hydrogen or hydrocarbon fuels. In both cases, simple electrochemical reaction within the fuel cell membrane takes place. The membrane, made of Nafion, allows only the hydrogen ions (protons) to pass through while the electrons have to travel externally through the load. At the cathode the hydrogen ions re-combine with the oxygen molecules by catalytic reaction to form water while heat is produced. The presence of water in the membrane is essential to ensure proton conductivity of the Nafion. However, too much water degrades significantly

the fuel cell performance. Therefore, analysis of the water production and removal to achieve optimum water management is vital [1]. Various models have recently appeared in the literature for estimating the fuel cell operation. Early models have dealt with the modelling of the whole fuel cell system. More recently computational fluid dynamics models describing the air or mixture motion combined with phenomenological models for the electrochemical reactions and the modelling of the porous membrane have been published. For example, in [2] a model for water balance calculation in the membranes of polymer electrolyte fuel cells has been presented, taking into account the operating characteristics of the whole device. The overall amount of water was estimated, rather then the detailed two-phase flow dynamics. In [3] a 2-D flow mixture model was presented for simulating the transport of water in the cathode of proton exchange membrane (PEM) fuel cells. In this model, the formation and distribution of two-phase (air and water vapour) flow in the gas-diffusion layer and the gas channel was pre-

---

* Corresponding author.
E-mail address: m.gavaises@city.ac.uk (M. Gavaises).

dicted as function of the current density, membrane properties and operating conditions. In a more detailed study [4], a 2-D CFD model for describing the electrochemical kinetics, current distribution, hydrodynamics and multi-component transport in hydrogen PEM fuel cells was presented and emphasis was given on the prediction of the hydrogen dilution effects when the reformate gas was used as the anode feed. In [5] a model for simultaneous calculation of water vapour flow inside the porous material as well as inside the gas channel was presented. Electroosmotic and diffusion fluxes were used to calculate the transport of water through the porous material. In [6] a model for the transport of the reactants and products in PEM fuel cells has been used to investigate the operating limits of PEM fuel cells using the unsaturated flow theory, which assumes uniform pressure across the entire porous layer. In [7,8] a fully 3-D model simulating the species transport and the reactions in both the anode and the cathode gas channels, the catalyst layer and the proton exchange membrane have been modelled, while in [9] emphasis was given in coupling the flow field with the heat generated during the electrochemical reaction and the local current distribution. However, all of the above studies do not consider the detailed mechanism of water droplet formation on the surface of the gas-diffusion layer and its interaction with the cross-flowing air. Additionally, the details of the design of the bipolar plates are not addressed in those studies although it is now well recognised that it is one of the key components in PEM fuel cells. In a recent study towards this direction [10], various flow field layouts inside bipolar plates are reviewed, in connection with the structure of the porous material. Although macroscopic flow details are found important, the detailed water droplet formation and transport dynamics is not addressed. It is however evident that the detailed multi-phase (air and water liquid) flow processes, as determined by droplet formation, detachment and further motion may require further attention. Fairly recently, two publications [11] and [12] are dealing with diagnostic and modelling tools for characterising the detailed liquid water formation, transport and distribution in fuel cells. From those studies it is clear that non-uniform liquid water distribution areas can be realised, as function of the operating details and the design of the bipolar plate, with significant implications on the performance of the cell. It is also evident that the structure of the porous material affects the liquid flow. Detailed investigation on the modelling of single-phase flow through porous materials has been presented in [13] and [14]. Still, those studies do not account for the air–liquid two-phase flow and are only limited to the flow inside the porous material without connecting it with the water flow emerging on the surface of the porous material. As part of this study, it will be demonstrated that during the operation of PEM fuel cells, the water produced from the electrochemical reaction between hydrogen and air, is transported through the porous membrane forming distinct droplets on the gas-diffusion layer (GDL) surface. Those droplets as they become larger and larger may be detached by the air flowing around them. This particular flow process has not been thoroughly investigated in the past, particularly its implications on fuel cell operation. In general, the wetting and detachment of liquid droplets from solid surfaces

when exposed to a cross-flowing air stream is of importance not only to fuel cells but also to a number of physical systems and engineering devices. Despite that, little information is available on the detailed dynamics leading to removal of droplets attached to solid surfaces. The problem is closely associated with the estimation of the adhesion forces acting between the solid–liquid–gas interface contact-line. It is well known [15] that the static and the dynamic contact angles between different materials together with the surface tension can serve as a macroscopic measure of the magnitude of those forces. Some studies have focused on modelling the flow of droplets or liquid films on surfaces. For example, in an early study presented in [16] a lubrication theory model was presented for studying the motion of small fluid droplets on a surface. In a more detailed study of [17], the shape of droplets attached to solid horizontal or inclined surfaces was modelled under steady-state conditions and by using analytical techniques. The contact angle value around the contact line was identified to be one of the most important parameters. The studies presented in [18] and [19] are closer to those to be reported here, in the sense that water droplets found inside another liquid—rather than air—are removed from either smooth or rough surfaces under the influence of a shear flow. The problem was analysed in terms of important dimensionless numbers, such as the Bond and the capillary number, and it was concluded that droplets may be detached if a newly introduced dimensionless parameter was greater than an experimentally determined limit. In [20] the thermodynamics of microscopic contact interactions between emulsion droplets and interfacial tension have been analysed and the important role of the deformability of liquid droplets relative to solid particles was investigated. Important parameters of relevance to PEM fuel cells, such as the concentration of surfactants, pH, ionic strength, temperature and droplet size have been considered. Still, the analysis was based on thermodynamic principles rather than detailed fluid dynamics. In [21] an experimental study recording the impact of droplets undergoing critical detachment from the solid surface was reported. Although not directly related to flow conditions in the air channel of fuel cells, this study has shown than critical deceleration/acceleration of the droplet can lead to liquid detachment, and thus, highlighting the importance of dynamic—rather than static— models to be applied to the prediction of detachment of droplets attached to solid surfaces. Experiments on droplets moving on chemically reacting porous surfaces have been reported in [22] showing formation of various flow regimes. The critical detachment force of a droplet wetting a disc in a pulsed extraction column has been studied experimentally and numerically in [23]. The adhesion force was estimated on the basis of hysteresis (dynamic) contact angle measurements. The authors have concluded that removal of the droplet from the plate is not predictable without a complete modelling of the dewetting dynamics accounting for the droplet sliding and the dynamic contact angle change. Indeed, this approach has been considered by the model to be presented in this work! Experimental data for the adhesion tension, contact angle and contact angle hysteresis of surfactant-laden droplets deposited on various solid surfaces have been reported in [24], highlighting the

importance for obtaining such information for every particular system under examination, since a wide range of values exist. Additional effects of pH and ionic strengths on aqueous media and hydrophilic or hydrophobic surfaces have been reported in [25]. Experimental results on critical wetting transition from a droplet to a thin liquid film as a result of a metastable surface state and an accompanying contact angle hysteresis has been reported by [26] and [27] and a Monte Carlo simulation of the transition from partial to complete wetting conditions has been presented in [28]. A theoretical model for predicting the magnitude and onset of capillary and dry adhesion forces in the presence of nano-scale roughness has been presented in [29] and validated with direct measurements of surface forces using atomic force microscopy. This study has suggested that it is the smaller scale of roughness that primarily controls the adhesion of surfaces. This has been found to decrease significantly with an increase of the surface roughness. This important finding is believed also to have implications on the present study, as it will be clear in a following section. Experimental techniques to measure heat flux, contact angle, shape and growth rate of condensing sessile droplets have been presented in [30] while thermodynamic models have been employed to describe those processes. One of the few studies investigating the detailed fluid dynamics processes of droplets moving on solid surfaces is presented in [31]. Both experiments and CFD numerical investigations have been performed to study the basic physics of moving micro-droplets on solid surfaces subjected to temperature gradients. The change of dynamic receding/advancing contact angles around the solid–liquid–air contact line have been found to be key parameters determining the behaviour of the micro-droplet. Although one of the few relevant studies reported so far to use detailed CFD tools, this study is not considering the transition from non-moving to moving conditions. The spreading and absorption of a droplet on a thick porous substrate has been modelled in [32] using elements of the lubrication theory and a finite element solver. The advantage of this study is that it considers the penetration of the liquid into the porous material. Darcy's law has been used to account for the discontinuous transition from saturated to unsaturated regions in the substrate and evolution equations for the droplet profile inside and outside the porous material have been derived. On the other hand, this study again is not addressing the transition from non-moving to moving conditions. Finally, in [33] the transition from static to moving conditions is studied using phenomenological rather than detailed computational fluid dynamics models. A force balance is employed to describe the condition of droplet detachment and their relative magnitude once the droplet is moving.

The present study aims to bridge a gap in simulating the detachment of liquid droplets from solid surfaces. A purpose-built transparent test PEM fuel cell has confirmed that single-droplet formation and detachment from the porous material surface is the main water flow mechanism taking place in the cathode channels. To describe the detailed flow distribution in such condition, the multi-phase flow equations describing the liquid–air interface dynamics [34] are solved on a Eulerian frame using a RANS flow solver. Since those models require

as input the static and dynamic contact angles formed at the solid–liquid–air interface, a parallel experimental programme was performed in order to obtain those data for materials of relevance to automotive PEM fuel cells. Measurements of the static and dynamic contact angles reported here for carbon-based porous materials used in PEM fuel cells are new in the searched open literature. Those have been obtained in a test air-channel under well controlled and monitored flow conditions. In addition, the measured separation line distinguishing between the non-moving and moving liquid droplet conditions is also reported. The dynamic process of droplet shape deformation before detachment from the surface, as visualised with a CCD camera, is additional information obtained as part of this study and used for validation of the developed computer model. Incorporation of dynamic contact angle change as part of the numerical solution has allowed for relatively successful predictions of the experimental observations of the droplet shape at different air velocities. At the same time, incorporation of the observed dynamic advancing and receding contact angles just before droplet detachment into the model has allowed successful prediction of the separation line for the different porous materials tested. Parametric studies highlight the relative influence of various parameters of importance to the detachment process of droplets from the solid surface. In the next section, the numerical methodology is described followed by the description of the experimental set-up. The results obtained are then described followed by the most important conclusions.

2. Numerical model

In this section, the two-phase flow governing equations are given with a brief description of the method used for their numerical solution is given. Since detailed description can be found in [35] and [36], emphasis here is given in the implementation of the adhesion forces methodology. The numerical methodology follows the finite volume method. The fluid domain is divided into control volumes represented by an unstructured grid refined at the interface between liquid and air. The volume of fluid (VOF) methodology is based on the introduction of a scalar variable α which is defined as the cell volume fraction occupied by the second fluid, which for this case is the liquid phase:

$$\alpha = \frac{\text{cell volume occupied by water}}{\text{total volume of the control cell}}. \tag{1}$$

The variable α is commonly referred to as volume fraction or indicator variable. It is evident that α take values between 0 and 1. Ideally α should take only those 0 and 1 values but because the numerical grid is not following the droplet shape, the liquid–gas interface is not indefinitely thin. Thus, a transitional area exists where the volume fraction variable α lies between 0 and 1. The governing equations are the Navier–Stokes momentum and continuity equations:

$$\frac{\partial \rho}{\partial t} + \nabla \cdot \rho \vec{u} = s_{\text{mass}},$$

$$\frac{\partial}{\partial t}(\rho \vec{u}) + \nabla \cdot \left(\rho \vec{u} \otimes \vec{u} - \bar{T}\right) = \vec{s}_u + \vec{f}_\sigma,$$

$$\frac{\partial}{\partial t}(\rho \varphi) + \nabla \cdot (\rho \varphi \vec{u} - \vec{q}) = s_\varphi. \tag{2}$$

An extra equation is solved for the volume fraction variable, which is of the form:

$$\frac{\partial \alpha}{\partial t} + \nabla \cdot \alpha \vec{u} = 0. \tag{3}$$

The flow fluid field is solved for the two phases simultaneously, where the fluid's properties are calculated with linear interpolation using the volume fraction variable α:

$$\rho = \alpha \rho_2 + (1 - \alpha) \cdot \rho_1, \qquad \mu = \alpha \mu_2 + (1 - \alpha) \cdot \mu_1. \tag{4}$$

Using the above equations and assuming that the two fluids are incompressible, the continuity equation is reformulated in its non-conservative form. The existence of a transitional area, where the volume fraction variable α lies between 0 and 1, enforces the use of the continuum surface force (CSF) model in order to calculate the interface curvature and the force arising from the surface tension inside the transitional area. Using this approach the mean curvature of the interface is calculated as:

$$\kappa = -\nabla \cdot \left(\frac{\nabla \alpha}{|\nabla \alpha|}\right). \tag{5}$$

And thus the force due the surface tension incorporated in the momentum equations is calculated as:

$$\vec{f}_\sigma = -\sigma \kappa \cdot \vec{n} = -\sigma \cdot \left(\nabla \cdot \left(\frac{\nabla \alpha}{|\nabla \alpha|}\right)\right) \cdot (\nabla \alpha). \tag{6}$$

For the solution of the above flow equations, an in-house CFD model (GFS) has been used. Special treatment is given to the calculation of the VOF equation in order to minimise diffusion, so that the transitional liquid–gas region is kept as narrow as possible. This is achieved by using appropriate discretisation method [35] as well as unstructured numerical grids and employing adaptive local grid refinement at the droplet interface. The refined cells follow the motion of the liquid–gas interface. Additionally, the second order fully implicit Crank–Nicholson time scheme is employed using small time steps. The time step restriction is according to the local Courant number which is kept below 0.3. The grid arrangement is collocated, where all the unknown variables are stored in the centre of the computational cell. In order to avoid pressure–velocity decoupling problems, arising from the fact that pressure and velocities are calculated in the same location, the convective flux through each cell face is calculated using the modification proposed in [37] for Cartesian grids and extended here for generalised curvilinear coordinates. The key feature of this approach is that the velocity used to calculate the convective flux through a cell face, is not calculated by a linear interpolation of the adjacent cells velocities, but is modified to be directly linked to the two adjacent pressure nodes. Following this procedure, the SIMPLE pressure prediction-correction method [38] is used in order to derive the pressure equation from the continuity equation. The convective and normal diffusion terms are discretised using the BSOU scheme (bounded second order upwind [39]). The cross-diffusion terms and the second order derivatives are discretised using standard central difference scheme. These terms are moved to the right-hand side of the conservation equation, and are treated explicitly in the iterative procedure. The set of the linear equations that result after the discretisation of the conservation equations are solved iteratively using a preconditioned conjugate gradient method solver. The porous material has been considered impermeable in the model. Therefore, the effect of capillary forces and water flow inside the porous material was not accounted. Finally, measured static and dynamic contact angle values for different porous materials have been used here as input to the computational model.

As mentioned, emphasis here is placed on the numerical treatment of the dynamic change of the contact angle during the deformation of the droplet surface under the influence of the air flowing around it. Surface tension is important part for calculating both the droplet deformation as well as the adhesion forces. The contact angle (or wetting angle), θ, is a quantitative measure of the wetting of a solid by a liquid. It is defined geometrically as the angle formed by a liquid at the free phase boundary where the liquid, gas and solid intersect as shown in Fig. 1. It can be seen from the figure that low values of contact angle indicate that the liquid spreads, or wets the surface, while high values indicates poor wetting. As clear, zero contact angle represents complete wetting and formation of liquid film on the surface. If the three-phase (liquid–solid–air) boundary is in actual motion the angles produced are called dynamic contact
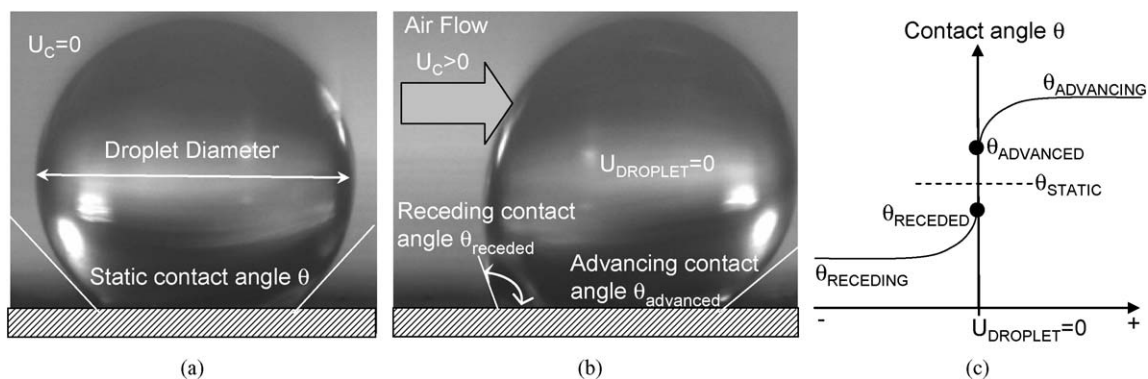

Fig. 1. (a) Contact angle of a non-moving liquid droplet in equilibrium with a horizontal surface surrounded by a non-moving gas, (b) contact angles of a non-moving liquid in equilibrium with a horizontal surface surrounded by a moving gas and (c) definition of static and dynamic receding and advancing contact angles.

angles and are referred to as 'advancing' and 'receding' angles. The difference between 'advanced' and 'advancing' as well as 'receded' and 'receding' contact angles is that those angles are realised at static droplet condition rather than in actual liquid motion but at a deformed shape deviating from the spherical. Actual values of those angles depend on the combination of the solid material and liquid and have to be determined experimentally. Here, both the static contact angle of Fig. 1a, as well as the 'advanced' and 'receded' angles of Fig. 1b, are reported in the following section. Those will be referred to as 'receding' and 'advancing' contact angles, although the actual ones, defined when the droplet is moving, may be different as the schematic of Fig. 1c indicates. Adhesion forces macroscopically can be seen as the result of the imbalance of surface tension forces at the solid–liquid–air boundary. Let σ_{lg} denote the interfacial tension due to the liquid–gas surface, σ_{sl} to refer to the interfacial tension due to the solid–liquid surface and σ_{sg} to indicate the interfacial tension of the solid–gas surface. In thermodynamic equilibrium the static contact angle θ_{st} is given by Young's law:

$$\sigma_{sg} = \sigma_{sl} + \sigma_{lg} \cos \theta_{st}. \tag{7}$$

In reality dynamic contact angles are associated with a moving contact line. They depend on the velocity U_c of the contact line. If one considers the advancing dynamic contact angle $\theta_{d,a}$ ($U_c > 0$) and the receding dynamic contact angle $\theta_{d,r}$ ($U_c < 0$), then the following outcomes exist. If $U_c = 0$, there is equilibrium, and the integral force acting on the contact line is vanishing:

$$F_d = \sigma_{sg} - \sigma \cos \theta_{st} - \sigma_{sl} = 0. \tag{8}$$

If $U_c < 0$, the contact line recoils and the uncompensated force F_d, acting on the contact line pulls the contact line towards the direction of the negative velocity:

$$F_d = \sigma_{sg} - \sigma \cos \theta_{d,r} - \sigma_{sl} < 0. \tag{9}$$

If $U_c > 0$, the contact line advances and the uncompensated force F_d, acting on the contact line is directed towards positive velocity:

$$F_d = \sigma_{sg} - \sigma \cos \theta_{d,a} - \sigma_{sl} > 0. \tag{10}$$

Combination of the last three Eqs. (8), (9) and (10) gives:

$$F_d = \sigma (\cos \theta_{st} - \cos \theta_{d,r}) < 0, \quad U_c < 0,$$
$$F_d = \sigma (\cos \theta_{st} - \cos \theta_{d,a}) > 0, \quad U_c > 0. \tag{11}$$

The contact angle also changes around the periphery of the droplet. The variation of the contact angle around the droplet periphery between the advancing and the receding value is assumed to follow a sinusoidal law. The static value is used at 90° (middle of the droplet) where the mean air velocity is parallel to the liquid–solid contact line. Integration of these forces around the periphery of the droplet produces a force F_w that opposes to the movement of the droplet (adhesion force). Thus, its direction is opposite to the direction of aerodynamic pressure force F_d acting on the droplet as a result of the non-uniform pressure distribution around it. In this study, the following numerical approach has been adopted for estimating the change of

the contact angle as the droplet is gradually deformed but still remaining in contact with the wall surface. Initially, the static angle is considered all around the liquid–solid contact line in the absence of air stream. As air velocity starts to increase, the liquid surface also starts to deform as a result of the air flowing around it. The resulting 'new' contact angles are calculated on the contact line from the slope of the VOF at the wall boundary cells. Since there will be an imbalance of pressure and adhesion forces relative to the previous droplet shape and the contact angle values of the previous time step, this 'new' value of the estimated contact angles are used to update the contact angle values used as input in the solved equations. Then, an iteration procedure is performed until droplet static equilibrium at this local condition is achieved. The maximum input value of the advancing and receding contact angles that is allowed to be given to the solved equations are the ones determined experimentally and corresponding to the $\theta_{receded}$ and $\theta_{advanced}$ values. Once the droplet shape is deformed to angles larger than those maximum observed limits, there will be an imbalance of forces and the liquid will start to move. That condition effectively corresponds to critical capillary number required for droplet detachment and defined the point at which the 'separation line' between nonmoving and moving condition is determined. This dynamic update of the contact angles during the solution procedure and its variation around the droplet periphery is the main new point of the numerical methodology used here. This methodology has allowed prediction of the observed droplet shapes as the droplets deforms before actually detaching from the surface, as well as the experimentally determined separation line.

3. Experimental

In this section, the experimental system used to obtain the required data for validating the developed computer model is described. Initially, the transparent test fuel cell is described. From this experiment, the water formation process on the GDL surface of the PEM fuel cell was identified. Then, the simple single-droplet test rig used for measurements of the liquid contact angles and the separation line is given.

3.1. Fuel cell experimental set-up

For visualising the water flow within the air channels of the fuel cell, a single-stuck transparent model has been constructed. The basic components are shown in Fig. 2. It consists of the MEA and the bipolar plates attached to the two sides where the hydrogen and air are flowing inside their channels. The air endplate was modified in such a way that a Plexiglas window was attached on the plate and being in direct view with the MEA. That has allowed images of the water emerging from the membrane and forming droplets on the GDL surface to be taken using a high speed camera. The experimental set-up for droplet visualisation in the fuel cell is illustrated in Fig. 3. It consists of the air source, hydrogen cylinder, air pressure controller, air/hydrogen inlet and outlet flow meters, air outlet humidity sensor and the transparent fuel cell. The width and depth of the air channel are 1.46×0.28 mm, respectively. In addition to
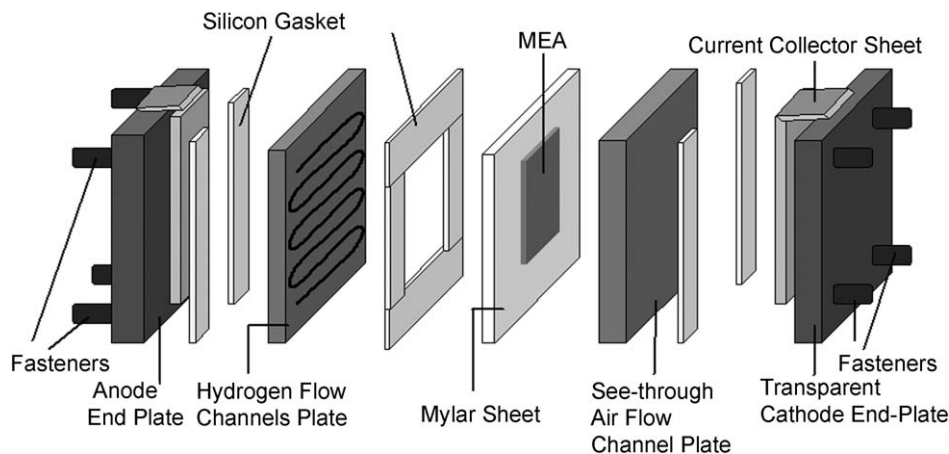
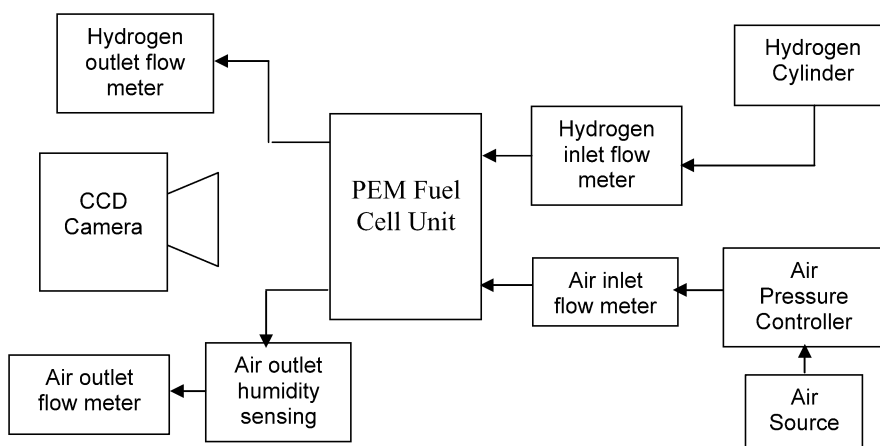Fig. 2. Components of the single-stack transparent fuel cell.

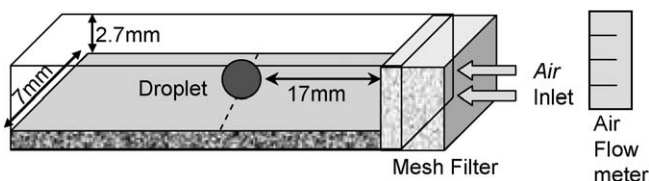Fig. 3. Experimental set-up for droplet visualisation in the fuel cell unit.

Fig. 4. Experimental set-up for single-droplet experiment.

droplet images, the air and hydrogen flow rates, hydrogen consumption, air humidity at the inlet and exit of the cell, voltage produced and load have been simultaneously recorded. Here, those results are not presented and only images of the water droplet captured using a high speed CCD camera will be shown.

3.2. Single-droplet and air channel experimental set-up

In order to visualise the behaviour of single droplets placed on the surface of different porous materials under controlled conditions independently of the fuel cell operation, a simple test-rig has been set-up, and it is shown schematically in Fig. 4. It consists of an air supply unit, an air mass flow controller, a high resolution CCD digital camera connected to a PC for image processing and finally the transparent air channel unit. The dimensions of the air-channel are 2.7×7.0 mm in cross-section

and 51 mm long made from Plexiglas. Air was entering into the channel via a flexible tube firmly connected to an adapter followed by a mesh section to ensure uniform air flow distribution at the inlet of the channel. The exit of the channel was free, thus atmospheric pressure can be assumed at its exit boundary. The air mass flow controller at the inlet has maximum uncertainly of $\pm 5\%$ at full scale. The inlet air enters the channel with a temperature and humidity of $22.3\,^{\circ}\text{C}$ ($\pm 2\,^{\circ}\text{C}$) and 30% RH ($\pm 5\%$), respectively. At the exit of the channel, the air velocity was measured using a hot wire sensor with $\pm 3.3\%$ uncertainly at full scale, to ensure no air leakage and accurate velocity measurements by the flow meter. Also, it was made sure that there was no air leakage through the joints of the channel model; this was checked by pressuring the model and looking for leakage by soap water. The air flow Reynolds number was based on the channel hydraulic diameter (4.9 mm) and mean air velocity. Since the droplets that have been tested were removed from the surface at air velocities between 5 to 15 m/s, the corresponding Reynolds number is in the range of 1500–4500. The incoming air was delivered at steadily increasing rate. This increase was slow enough to ensure that possible dynamic flow effects influencing the droplet behaviour were minimal. A timer was used as a reference to ensure certain increase of the flow during a fixed time period. Droplets of sizes between 0.4 to

1.8 mm were manually generated with a help of load syringe and placed on the GDL surface around 17 mm downstream of the air inlet. Images of the droplet were obtained with a CCD camera using an exposure time of 1 ms. The record timing was set by triggering the camera externally using a pulse generator, to capture more than 50 successive real time images of the droplet shape deformation before its detachment from the surface. Post processing of the collected images has provided estimates of the static and the dynamic contact angles as well as plotting of the moving/non-moving separation line for different droplet-size air velocity values. Overall, more than 1000 water droplets of different sizes have been visualised. The testing procedure for each droplet was completed in three consecutive stages. The first stage involves drying of the GDL surface using an air hot gun. The surface was then kept for sometime in the ambient until it cooled down. The reason for that is to ensure similar operating conditions of surface dryness in each conducted test as surface wetability can vary the static and dynamic contact angles. The next stage was to produce a droplet with certain diameter and placed it at a specific location in the channel. The first image of the droplet was taken without air flow, to allow measurement of static contact angle. Those measurements are reported here for the different material tested while their mean value has been used as input for estimating the initial droplet shape used with the computational model. Then air enters into the channel with gradually increasing velocity and successive images of the droplet were taken while its surface shape was changing before its final detachment from the surface. The last image recorded before droplet detachment (zero mean droplet velocity) was used for estimating the dynamic advancing and receding contact angle values reported here. Those values were also used by the computational model for predicting the separation curve. The thickness of the porous materials tested was around 200 μm. To avoid (or minimise) water flow through the porous surface, the porous layer was glued on a piece of graphite having the same length and width. With this set-up, capillary forces and water flow inside the porous material can be neglected, justifying the assumption of impermeable wall adopted by the computer model valid. Three different commercial GDL materials were tested. Their surface structures, as visualised using a microscope are shown in Fig. 5. Those will be referred to in all following sections of this paper as 'carbon paper 1,' 'carbon paper 2' and 'carbon cloth.' It can be seen that their surface is quite irregular. No perfectly circular cross-section 'holes' can be seen on the surface structures. The size of the water flow passages is of the order of 50–100 μm. This is small enough compared to the size of the droplets tested, which was above 400 μm. Finally, the surface roughness was also measured for all three materials using the Telyserf Standard (Taylor Hobson) method. It was found to have an average variation of about 2 μm for the carbon cloth and about 2.5 μm for the carbon paper materials, respectively. The peak-to peak variation was of the order of 5 μm. Those values correspond to less than 1% relative to the droplet diameter roughness. Thus, in the computational model smooth surface has been assumed.

4. Results and discussion

4.1. Fuel cell water droplet formation

The main target of this experiment to be presented here refers to the identification of the water flow process taking place within the air channel of the transparent fuel cell. Fig. 6 shows a sequence of events of a water droplet emerging at a specific location on the GDL surface. The droplet is becoming larger and
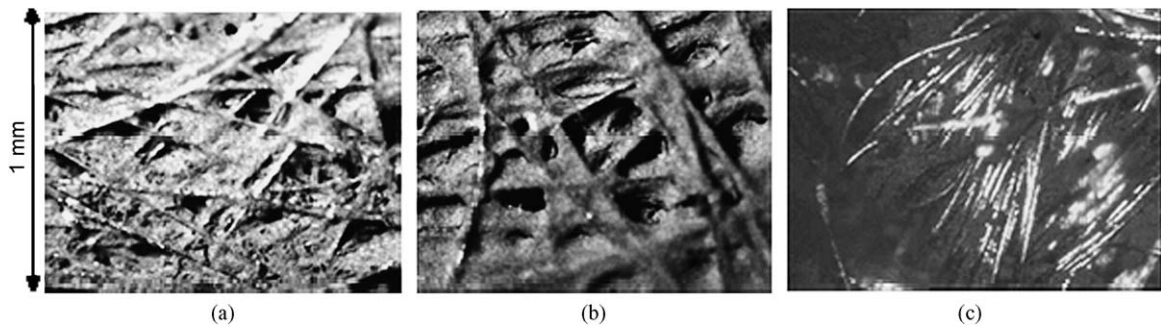

Fig. 5. Microscope photograph of the three diffusion layers tested (a) carbon paper 1, (b) carbon paper 2 and (c) carbon cloth.
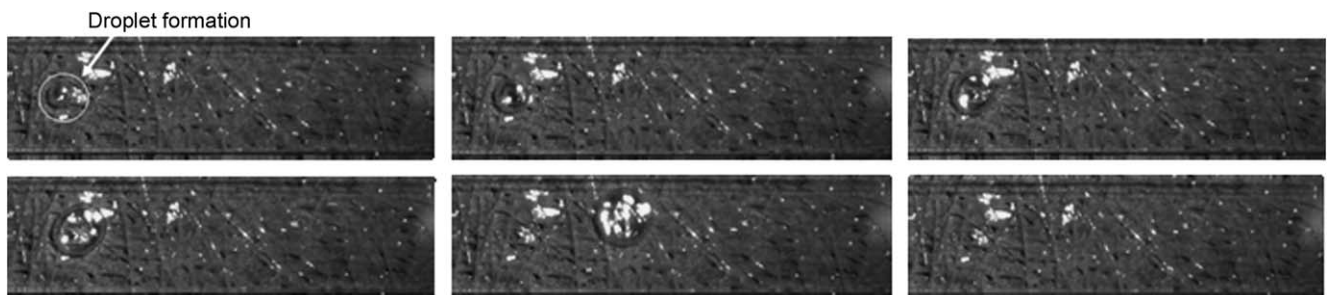

Fig. 6. Visualised water droplet formation and detachment from the GDL surface of the air channel of the transparent fuel cell.

larger gradually until suddenly detaches from the point of its formation and swept away by the flowing air. Conditions leading to formation of liquid film on the GDL surface rather than water droplets have not been observed. Recording of various operating conditions has led to the conclusion that formation of individual droplets on the GDL surface is the dominant mechanism of water flow within the air channel of this experimental fuel cell. As it is clear, with this transparent fuel cell only top-view but not side-view images can be obtained. Thus, contact angle measurements are not possible. Additionally, the local air velocity conditions, the pressure difference at the two sides of the GDL, the details of the water flow through the porous material, liquid evaporation, surface wetting and electric current flow are parameters may affect the droplet formation and detachment process. Since those parameters and their effect on static and dynamic contact angles is not easy to be determined experimentally, it was considered important to perform a simple experiment for validating the CFD model predicting the droplet deformation and detachment process from the GDL surface. It is expected that the complexity of all the above parameters will be macroscopically reflected on contact angle values and the separation line. The model can be then used for estimating the effect of all those parameters on the contact angles once the separation line for a specific fuel cell has been determined.

4.2. Contact angle measurements

As already mentioned the contact angle value under static and dynamic flow conditions is the parameter that has to be determined experimentally for defining macroscopically the adhesion forces as function of surface tension and surface wetting. Even if other operational parameters affect its value during the fuel cell operation, model validation has to be performed under controlled conditions but for the materials used in fuel cells. Measurement of static and dynamic contact angles has been obtained using the sessile drop method. In this method, a tangent was fitted to the three-phase point where the liquid touches the solid surface. By drawing from the tangent a perpendicular line to the solid–air interface, contact angles can be estimated. In the absence of air flow, the contact angle on the left and right side of the droplet were almost identical. As air flows through the channel, both angles start to change. The receding dynamic angle, in the side of incident air, decreases whereas the advancing dynamic angle increases as shown in Fig. 1b. From such images the static contact angle (defined as zero air velocity), and receding/advancing dynamic contact angles just before droplet detachment from the surface were obtained with a maximum uncertainty of ±1.1° in cases of the most blurred images, and a mean of ±0.5° for all droplets recorded. Fig. 7a shows the measured static contact angles for the three materials as function of droplet size. It can be seen that each material has a different static contact angle. Carbon paper 1 has the smallest static angles with a mean value of 120° while paper 2 and carbon cloth have a mean value of about 140° over the measured range of the droplet size. The peak-to-peak measured difference is of the order of 20° for the same material. It can be also seen that although the measurement points are quite scattered within those
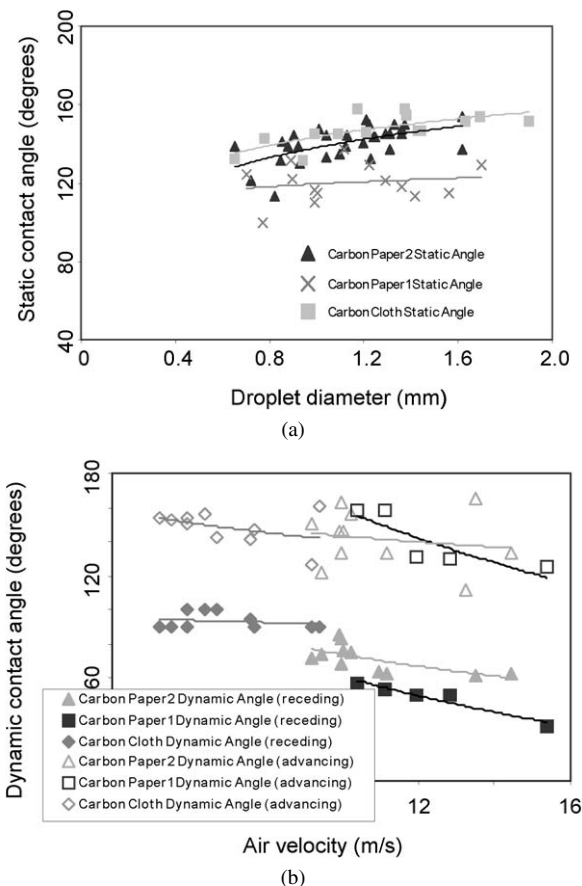

Fig. 7. (a) Measured static contact angles as function of droplet sizes and (b) measured advancing and receding contact angles as function of mean air velocity, for the three different GDL materials.

20°, the static contact angle increases slightly with increasing droplet size. This implies only a small influence of gravity on the initial droplet shape under static conditions. As mentioned, this macroscopic information was used as input to the computational model, together with the advancing the receding contact angles just before droplet detachment. Sample values are shown in Fig. 7b, but this time as a function of the mean air flow velocity. The results show a large difference in the contact angles for the three materials tested. Especially, the receding angles can vary as much as 50° between them. Those differences are expected to result macroscopically to different separation curves for the three materials. The carbon cloth shows the larger value, which corresponds to the smaller change relative to static conditions, or to smaller droplet deformation. It is thus expected that for this material smaller air velocity will be needed to remove the droplet from its surface. Another parameter that was specified from the images was not only the static contact angle value but also the deviation of the droplet shape under static conditions from the spherical one. The dimensionless Bond number, defined as $Bo = \rho_1 \cdot g \cdot D_d^2 / \sigma$ can be used to express the influence of gravity on the static droplet shape for different droplet sizes and surface tension values on a normalised plot. For the given surface tension, density and droplet size between, 0.4–1.8 mm the corresponding Bond numbers are in the range of 0.025–1.0 Since in order to appreciate any significant effect of

gravity, the Bond number should be above 2.5 [40], only minor influence is expected. Deviation from the spherical shape is becoming clear in Fig. 8. This figure presents the ratio between the observed droplet-wall contact length, normalised with the droplet diameter, against the measured static contact angle for the three materials tested. Although one would expect a sinusoidal variation of this ratio with the static contact angle, the recorded values look randomly scattered. The deviation from the spherical shape was found to be bigger for the two carbon papers.

4.3. Droplet detachment process and model validation

Having determined the physical parameters required by the numerical model for estimating the adhesion forces, the validation cases of the computer model are presented. Fig. 9 shows the test case used for simulating the flow process within the air channel. The initial numerical grid is shown in Fig. 9a. As can be seen, the unstructured mesh is refined at the liquid–gas interface while this refined area moves together with the droplet surface once this starts moving, as shown in Fig. 9b. All droplets simulated have initially spherical shape (gravity is neglected)
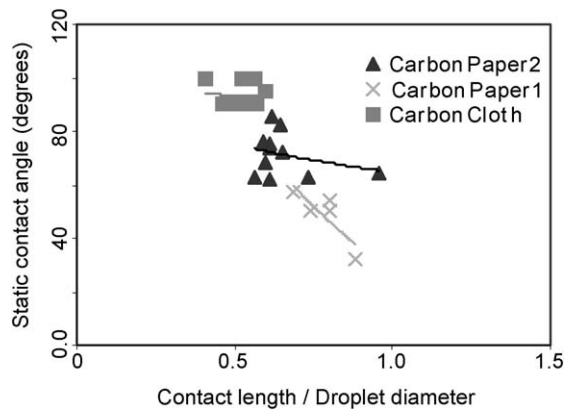

Fig. 8. Recorded ratio between normalised droplet-wall contact-length against the measured contact angles for the three materials tested.

and cross the solid wall with the measured mean static contact angle of each different carbon material. The dimensions of the cross-section of the air channel simulated are identical to those of the test air channel of Fig. 4. At the inlet, uniform air velocity is used while at the exit, located at about 50 droplet diameters from the droplet location, fully developed flow has been assumed. Different grid sizes have been initially tested. From those initial runs it has been concluded that using approximately 150,000 cells are adequate to capture the dynamic change of the shape of the droplet. The cell spacing on and around the droplet surface was about 5–10 μm. The initial air velocity was set to increase linearly from quiescent conditions to its maximum value corresponding to the separation velocity within approximately 30 ms. Simulations performed using faster or slower rates of increase for the inlet air velocity have confirmed that this value can be considered slow enough not to induce significant instabilities on the droplet surface deformation and not to affect the separation process of the droplet. Physical properties (density, viscosity and surface tension) of air and water were taken at 1 bar and 20 °C. Table 1 shows the static and dynamic contact angle values used. Due to Courant number restriction of the computational time step, the corresponding calculation time was approximately 2–3 days of CPU time on a typical high-end PC. In total 6 calculation points (initial droplet size) have been used to predict the separation curve for each GDL material. Fig. 10 presents sequence of events of a 1.0 mm droplet deforming before actually detaching from the GDL surface. Both, CCD images and the corresponding CFD model predictions are shown. It is clear that the droplet becomes significantly deformed before actually 'flies' from the surface. This term is introduced here in order to denote the sudden loose of contact between the water droplet and the solid surface. At a specific air velocity, its deformation reaches the maximum measured advancing and receding contact angles. Once this happens, the droplet suddenly detaches from the surface and 'flies' over it with a velocity high enough to set it out of the viewing area of the camera. The numerical model seems to predict a similar sequence of events. More careful inspection of the computational results reveals that the droplet surface ac-
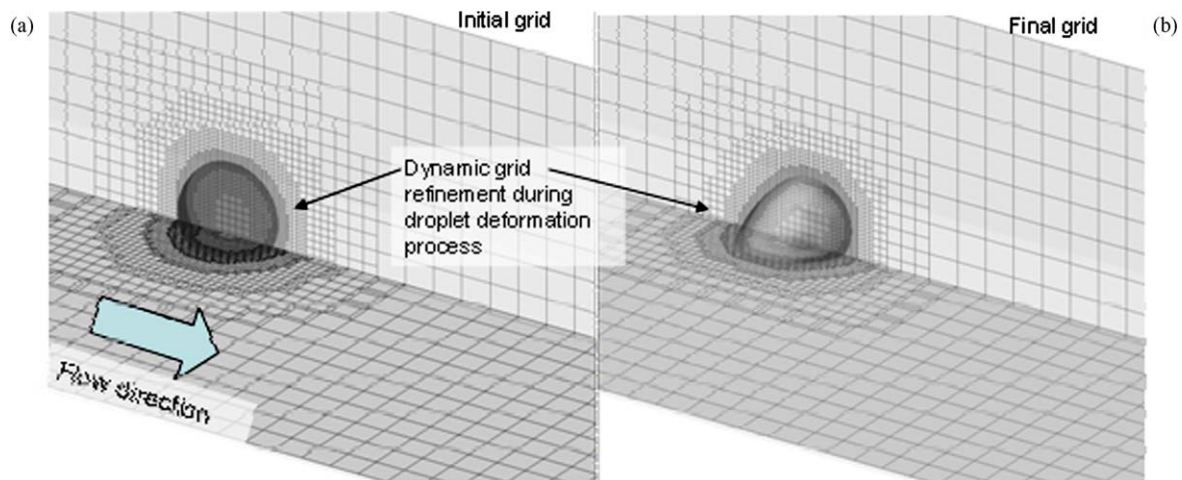

Fig. 9. Numerical grid with adaptive local grid refinement on the droplet surface for the (a) initial droplet position and the (b) droplet position just before detachment from the surface.

tually performs a vibration before detaching from the surface. This was more evident in cases where the air flow velocity was not high enough to sweep it. In those cases, the droplet was deformed but without reaching the maximum advancing and receding contact angles. A vibrational motion of the droplet shape until stabilising to its final shape was calculated and also observed. Such dynamic droplet shape effects amplified by variable air flow velocity can significantly affect the separation line, but are not further reported here. Fig. 11 compares the calculation results of two different droplet sizes but with the same static and dynamic contact angles. The rendered droplet surface is transparent so the flow field inside it can be also seen, simultaneously with the air flow distribution around the droplet. The pictures reveal that the overall shape of the droplet is less deformed when its size becomes larger. This result was expected, since the projection area of the droplet to the flowing air is larger and thus, the pressure force acting on it is relatively larger with increasing droplet size for the same value of the mean air velocity. Recorded shapes of five sample droplets, normalised with the droplet diameter, and obtained just before detachment takes place, are shown on Figs. 12a and 12b, for the carbon cloth and the carbon paper, respectively. On the same plot, the calculated droplet shape is also shown, using as input the measured mean contact angle values. As can be seen, the visual edge of the droplets varies between them, possibly due

to the difference in the initial droplet size. Differences seem to be larger for the droplets placed on the carbon-paper material. For both materials, the calculated droplet shape falls within the observed droplet shapes.

The air velocity at which the droplets will actually loose contact with the wall was also recorded. This correlation is reflected on the separation line. Fig. 13 presents the measured values of mean air velocity and corresponding droplet size at which the droplet is loosing contact from its initial position. As already mentioned, this line is referred to as the 'separation line.' To the left of this line, the droplet remains on the wall while to the right it is detaching from the surface. It can be seen that for the three different materials tested, significantly higher air velocity values are required to move the droplet. As already explained, this is directly related to the different contact angles for those different materials. Droplets were faster removed from the carbon cloth. As mentioned in the previous section, for this material the smallest receding contact angle difference from the static condition were recorded. On the same graph, the corresponding predicted values are also plotted. It seems that the model reflects the different contact angle input values on the predicted separation curve. At the same time, the predicted separation curves follow the same slope as the experimental data for different droplet sizes. The biggest difference between model predictions and experimental data for the separation line is found for carbon paper 1, possibly because for this material the largest deviation of the initial droplet shape from the spherical was recorded. From this comparison between model predictions and experimental values, confidence on the developed numerical methodology was established. It was then considered important to perform parametric studies to examine the effect of various parameters on the separation line. These are presented in the following section.

Table 1
Contact angle values used for the prediction of the separation line for the different GDL materials tested

Case A	GDL material	Contact angle (degrees)		
		Static	Advancing	Receding
	Carbon paper 1	125	140	50
	Carbon paper 2	130	140	70
	Carbon cloth	145	150	90

$U_{air}=0\,m/s$ $U_{air}=8\,m/s$ $U_{air}=11\,m/s$ $U_{air}=13\,m/s$

(a)

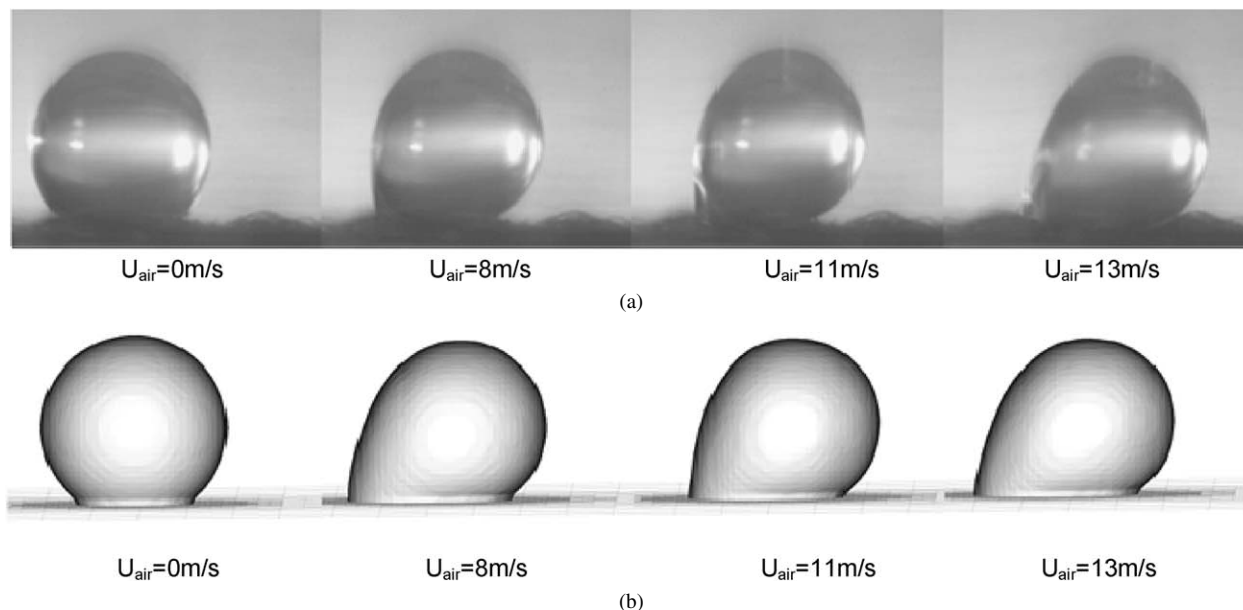$U_{air}=0\,m/s$ $U_{air}=8\,m/s$ $U_{air}=11\,m/s$ $U_{air}=13\,m/s$

(b)

Fig. 10. (a) Photographed and (b) predicted sequence of surface distortion of a 1.0 mm droplet before detachment from carbon cloth surface.
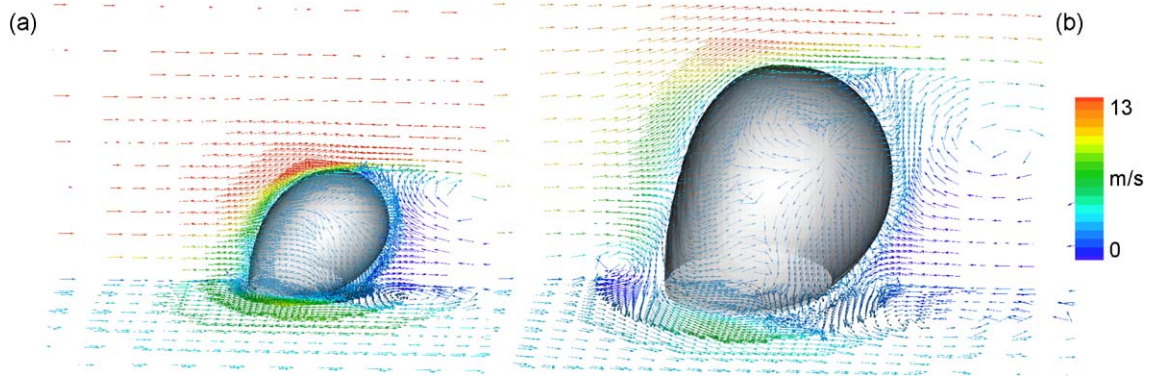
Fig. 11. 3-D view of calculated droplet shape and flow field around and inside a (a) 0.8 mm droplet and (b) 1.2 mm droplet and 13 m/s mean air velocity.
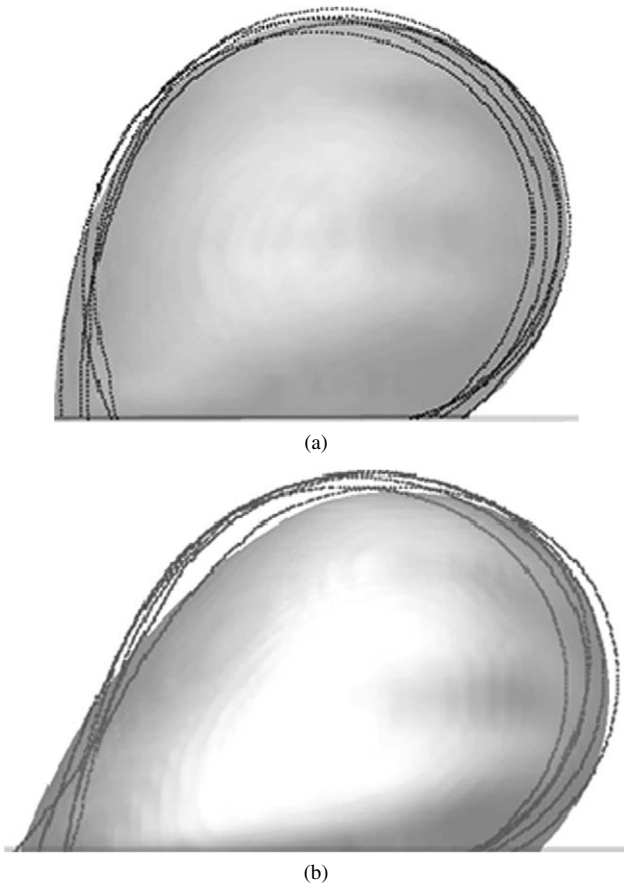

(a)

(b)

Fig. 12. Comparison between calculated droplet shape before detachment and visual edge of various 1.0 mm droplet 'terminal' shapes placed on (a) carbon cloth and (b) carbon paper.

4.4. Parametric studies on separation line

Clearly, many parameters can affect the separation line. These refer not only to use of different materials, which are critical, but also to operating and flow conditions. The effect of inlet air velocity profile and the droplet location within the air channel have been investigated experimentally. Additionally, the effect of water flow connecting the liquid droplet with the porous material, the effect of gravity and effect of water temperature and the simultaneous contact of droplets at surfaces with different contact angles have been examined using the numerical model. Fig. 14a shows the measured effect of the velocity
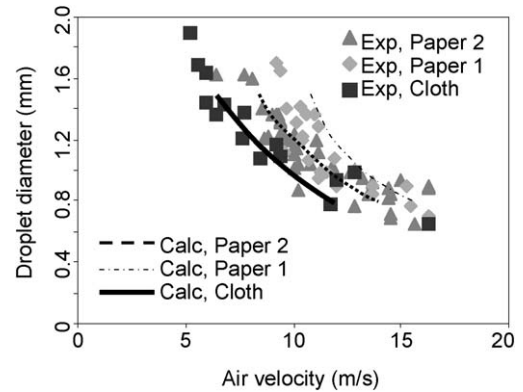

Fig. 13. Measured and calculated separation lines for the three different GDL materials.
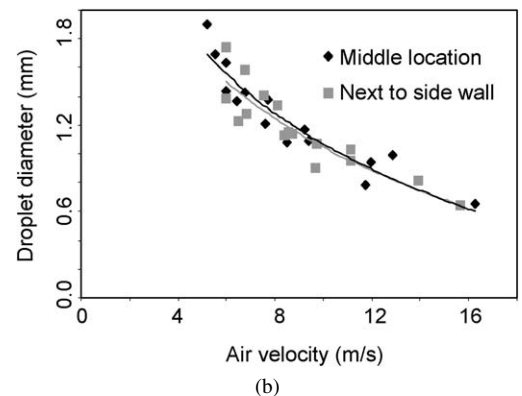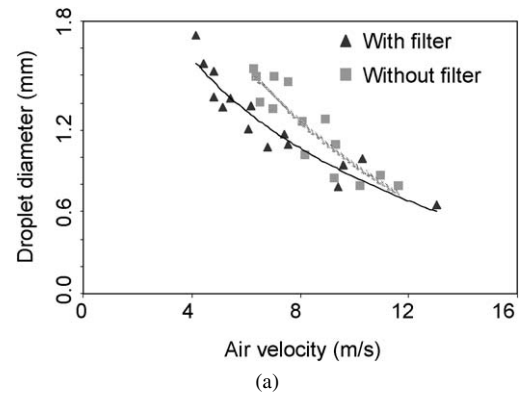

(a)

(b)

Fig. 14. Measured effect of (a) air flow inlet conditions on separation line and (b) droplet location within the channel on separation line.
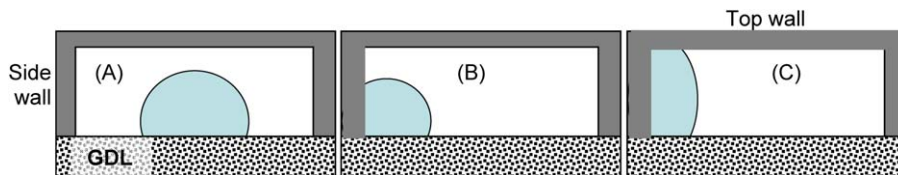
Fig. 15. Schematic of the three different cases investigated numerically (a) droplet at the middle of the channel, (b) droplet in contact with GDL and side wall and (c) droplet in contact with GDL, side wall and top wall.

Table 2
Contact angle values for the GDL material and the side-wall material used for cases B and C

Cases B and C	Solid surface material	Contact angle (degrees)		
		Static	Advancing	Receding
	GDL: carbon cloth	145	150	90
	Side: graphite	90	110	70

profile of the incoming air on the separation line using the carbon cloth material. The incoming air velocity distribution was modified by placing an air filter just at the pipe exit, which was creating a relatively uniform air velocity distribution upstream of the droplet. In the absence of this filter, it is expected that a short of parabolic or laminar flow or developing flow profile will be realised by the droplet. As can be seen, the droplet is easier swept by a uniform air velocity rather than a developing flow. This result is expected, since the droplet height relative to the channel was less than 1/3, implying that the actual velocity realised by the droplet when the air velocity was undeveloped would be smaller than its mean value. Fig. 14b shows the effect of placing droplets out of the symmetry plane (2.4 mm from the centre of the channel) but without touching the side wall. For this experiment, the mesh filter was inserted at the exit of the air pipe. As can be seen, once the air velocity profile entering into the test area is relatively uniform, the droplet location is not affecting significantly the separation line. This is expected to be the case within the air channel in fuel cells, where the long length of the channel and the presence of many droplets acting as 'obstacles' to the flowing air are expected to result to a relatively developed flow. It was also considered useful to use the computational model in order to examine the effect of the droplet location inside the air channel in the case it is initially in contact with the side wall of the air channel. A schematic of the cases investigated is shown in Fig. 15. As can be seen, two additional cases have been considered. In addition to Fig. 15a, which corresponds to all cases investigated so far, and which will be referred to as 'case A,' the 'case B' of Fig. 15b corresponds to a droplet in contact with the side wall and the 'case C' corresponds to a droplet in contact both with the side and the top wall. It is expected that the material of the side and the top wall surfaces is different from the porous material of 'case A,'

and thus, different contact angles have to be used, as shown in Table 2. The values assumed here correspond to contact angles between water and graphite, a typical material used in fuel cells. Those are significantly smaller than the measured ones between the water and the porous carbon materials. The remaining parameters tested are listed in Table 3. The first one corresponds to the influence of the water flow within the porous material. To simulate this condition, a cylindrical pipe filled with water was connected to the droplet, as shown in Fig. 16. Different pipe diameters of 50, 100 and 150 μm have been tested, which corresponds to 5, 10 and 15% of the droplet diameter at detachment. At the same time, various inlet velocity values at the inlet boundary inlet of those pipes have been simulated. Typical values have been estimated by applying the Darcy's law expressing the pressure drop within porous materials. For a typical porous material thickness of 200 μm, the corresponding pressure drop at its two sides is of the order of 0.0015 to 0.2 bar. Simulations have been performed assuming either that initially no liquid exists on the solid surface or that a liquid droplet preexists from the initiation of liquid inlet flow. For the latter case, the initial droplet size was slightly larger than the feed pipe diameter. Between those two different initial condition cases, no significant variations have been observed. The used inlet velocity values and feed pipe diameter correspond to significantly smaller liquid volume relative to the volume of the droplet at detachment during the computational time required for droplet deformation and detachment from the wall surface (about 30 ms). As the images presented in Fig. 16 show, although the liquid volume increases with time, the droplet shape is not affected by the incoming liquid as long as the air velocity flowing around the droplet is not strong enough to start causing significant deformation to its shape. This implies that this flow process is not fast enough to affect significantly the separation curve. Thus, any calculated differences are mainly attributed to the smaller friction area between the liquid droplet and the wall surface in the presence of the liquid connecting pipe rather than the internal liquid circulation induced by the incoming liquid flow. Finally the effect of two more parameters, the change of liquid surface tension, which can be realised by changing its temperature to that of the operating condition of 80 °C as well as of gravity, have been examined. Two directions for the gravity

Table 3
Variables and corresponding values tested for parametric investigation on the separation line

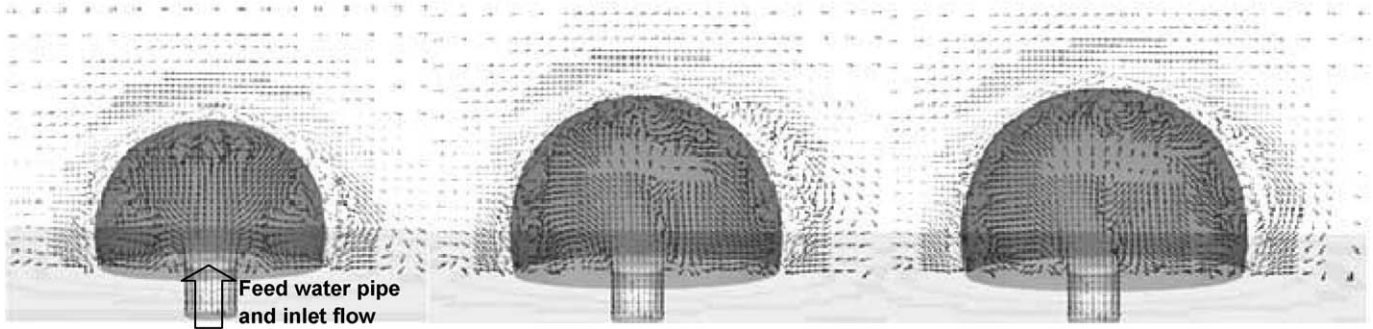| Feed pipe diameter (μm)	Feed inlet velocity (m/s)	Water temperature (°C)	Gravity (m/s^2)	
			Normal to GDL	Normal to U_{air}
50, 100, 150	7×10^{-4}, 7×10^{-3}, 3.5×10^{-2}, 0.1	20, 80	0, 9.81	0, 9.81

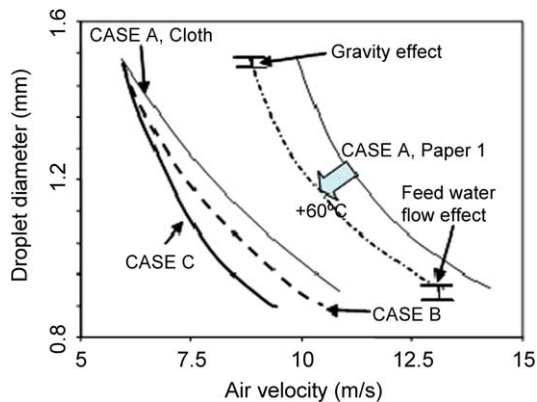Fig. 16. Predicted droplet shape during feed water flowing from inlet pipe.

Fig. 17. Plot summarising the effect of all parameters investigated numerically on the separation line.

acceleration vector have been tested, corresponding to two possible bipolar plate orientations. In the first case, gravity vector was normal to the GDL surface while in the second in was parallel to it and normal to the mean flow velocity, thus imposing a side force to the droplet. The effect of all those parameters on the predicted separation line is summarised in Fig. 17. On this graph, the lines predicted for 'case A' for the carbon cloth and carbon paper 2 and shown in Fig. 13 are also re-plotted. By comparing the different lines plotted, it can be seen that selection of a different GDL material is expected to have the strongest effect on the separation line. The influence of operating temperature is important, since it changes the liquid surface temperature. Decreasing surface tension values results not only to smaller adhesion forces but also to easier droplet deformation and thus faster removal from the solid surface. The effect of gravity as well of the incoming water flow is marginal for the range of conditions investigated here. Finally, contact of the liquid droplet with the side wall seems to significantly alter the predicted separation line. For the two curves plotted here corresponding to 'case B' and 'case C' the droplet diameter plotted is the equivalent droplet diameter. This has been defined as the diameter of the droplet having the same volume as that of the liquid present within the air channel. As can be seen, droplets are removed at lower velocities when in contact with the side or the top solid surfaces. Although that for the same liquid volume the total area of droplet with contact with the side wall and the porous material is proportionally larger when compared to 'case A' the contact area only between the liquid droplet and the

porous surface is about half. This results in almost half adhesion force between the liquid and the porous surface when compared between cases A and B. Considering that smaller contact angle values exist the side wall, this results to an overall smaller adhesion force in the direction of the mean flow the thus, faster droplet removal. In particular, the lost of symmetry relative in this case B has resulted in a much more complicated flow development process when compared to 'case A.' Fig. 18 presents a sequence of calculated events of a droplet initially in contact with the porous material, the side wall and the top surface. Its initial shape resembles more a semi-cylinder rather than a semi-spherical droplet. As can be seen, the liquid develops a neck close to the porous surface since there is an imbalance of forces acting around it. This results from the different contact angles used. The higher forces resulting on the contact between the water and the porous surface relative to those at the top surface, lead to the formation of this neck, which, as it develops may lead to complete separation of the droplet from the porous surface. It looks like that the droplet may 'climb' on the roof surface of the channel and form a film flow over the graphite material. Although not reported here, similar water droplet behaviour when coming in contact with Plexiglas has been also visualised.

5. Conclusions

Both calculations and experiments have been presented investigating the detachment of water droplets from carbon porous material surfaces under the influence of an air stream flowing around them. Visualisation of the flow in a purpose-built transparent test PEM fuel cell has revealed that the water produced within the MEA forms droplets on the surface of the gas-diffusion layers rather than liquid film, and which then, may be removed from the flowing air. The VOF method was selected as the CFD methodology for predicting the droplet surface deformation and further detachment from different GDL porous surfaces. This methodology was implemented within the frame of an in-house flow solver with the ability to handle fully unstructured meshes and incorporating adaptive local grid refinement at the liquid–gas interface. Experiments performed with a test air channel in which single droplets were placed on the same porous material surface as that used with the transparent fuel cell but under impermeable flow conditions, have indicated that the droplet shape changes dynamically from
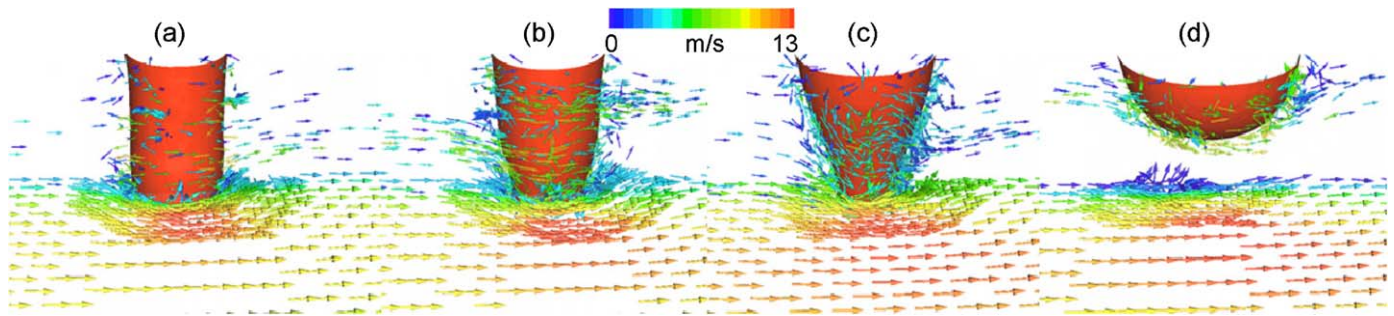
Fig. 18. Liquid droplet flow for 'case C' (initial contact with GDL, side wall and top wall surface), showing liquid detachment form the surface with the biggest adhesion force towards the surface with the smaller adhesion force.

its static position until it is finally loosing contact from the wall surface and swept away by the air. The static and dynamic contact angles have been measured for different droplet sizes, air velocities and porous materials. A numerical method for updating dynamically the advancing and receding contact angles during the numerical solution procedure until balance of aerodynamic and adhesion forces was achieved at specific air velocity has been used. This has allowed prediction of the droplet deformation process prior to its detachment from the wall surface. Additionally, use of the maximum measured values of the receding and advancing contact angles just at the time of droplet detachment from the surface, has allowed prediction of the separation line between non-moving and moving flow conditions. The results showed good agreement between model predictions and experimental data for three different GDL materials. Finally, parametric studies investigating the effect of various flow parameters on the separation line have been presented. In particular, the effect of the incoming air velocity profile and the droplet location within the air channel, have been investigated experimentally. The results have confirmed that uniform air velocity detaches the liquid droplets at lower mean air velocities. Once uniform flow conditions are established, the location of the droplet within the air channel is not affecting the separation line. However, if the droplet is initially in simultaneous contact with the side wall surface of the air channel and which have different contact angle from the porous material, then the separation line changes significantly. Model predictions have revealed that for these cases, the imbalance of adhesion forces at the two sides of the droplet results to liquid motion towards the smaller adhesion surface even in the absence of an air flow. Additionally, the effect of water flow connecting the liquid droplet with the porous material, the effect of gravity and the effect of water temperature have been investigated numerically. Out of these parameters, the temperature increase was found to shift the separation line towards lower velocity values, since the surface tension decrease at increasing liquid temperatures results to lower adhesion forces and easier droplet surface deformation.

Acknowledgment

Appendix A. Notation

α	Volume of fluid (also noted as indicator function) (–)
D	Liquid droplet diameter (m)
g	Acceleration of gravity (m/s^2)
$\vec{f}_\sigma$	Volumetric force due to surface tension (N/m^3)
$\vec{n}$	Vector normal to interface of the two phases (m^{-1})
$\vec{q}$	Diffusion flux vector of a general scalar variable (varies)
s_{mass}	Volumetric mass sources in the mass conservation differential equation (kg/m^3 s)
$\vec{s}_u$	Momentum sources in the momentum conservation differential equation (N/m^3)
s_ϕ	Volumetric sources in the conservation differential equation of a scalar variable ϕ (varies)
$\bar{T}$	Stress tensor (N/m^2)
t	Time (s)
$\vec{u}, U$	Velocity (m/s)
A	Area (m^2)
F	Force (N)
Bo	Bond number (–)

Greek symbols

θ	Contact angle (degrees)
κ	Curvature (m^{-1})
ϕ	Any scalar variable ϕ (varies)
μ	Dynamic viscosity (N s/m^2)
ρ	Density (kg/m^3)
σ	Surface tension (N/m)

Indices

1	Fluid 1 (gas)
2	Fluid 2 (liquid)
d, a	Advancing contact angle
d, r	Receding contact angle
st	Static contact angle
d	Droplet
c	Contact line
sl	Solid–liquid interface
sg	Solid–gas interface
lg	Liquid–gas interface

Abbreviations

VOF	Volume of fluid
GDL	Gas-diffusion layer
MEA	Membrane electrode assembly
CFD	Computational fluid dynamics
PEM	Proton exchange membrane
CCD	Charged coupled device
RANS	Reynolds averaged Navier–Stokes

References

[1] M.F. Mathias, J. Roth, J. Fleming, W. Lehnert, Technol. Appl. (2003).
[2] T. Okada, G. Xie, M. Meeg, Electrochim. Acta 43 (14) (1998) 2141–2155.
[3] L. You, H. Liu, Int. J. Heat Mass Transfer 45 (11) (2002) 2277–2287.
[4] S. Um, C.Y. Wang, K.S. Chen, J. Electrochem. Soc. 147 (12) (2000) 4485–4493.
[5] Z.H. Wang, C.Y. Wang, K.S. Chen, J. Power Sources 94 (2001) 40–50.
[6] U. Pasaogullari, C.-Y. Wang, Electrochim. Acta 49 (2004) 4359–4369.
[7] M. Hu, A. Gu, M. Wang, X. Zhu, L. Yu, Energy Convers. Manage. 45 (2004) 1861–1882.
[8] S. Um, C.Y. Wang, J. Power Sources 125 (2004) 40–51.
[9] B.R. Sivertsen, N. Djilali, J. Power Sources 141 (2005) 65–78.
[10] X. Li, I. Sabir, Int. J. Hydrogen Energy 30 (2005) 359–371.
[11] J. Stumper, M. Lohr, S. Hamada, J. Power Sources, in press.
[12] F. Barreras, A. Lozano, L. Valino, C. Marin, A. Pascau, J. Power Sources, in press.
[13] A.G. Yiotis, A.K. Stubos, A.G. Boudouvis, Y.C. Yortsos, Adv. Water Resour. 24 (2001) 439–460.
[14] K. Boomsma, D. Poulikakos, J. Fluids Eng. 124 (2002) 263–272.
[15] R.J. Hansen, T.Y. Toong, J. Colloid Interface Sci. 37 (1) (1971) 196–207.
[16] H.P. Greenspan, J. Fluid Mech. 84 (1978) 125–143.
[17] E.B.V. Dussan, R.T.-P. Chow, J. Fluid Mech. 137 (1983) 1–29.
[18] M. Mahe, M. Vignes-Adler, A. Rousseau, C.G. Jacquin, P.M. Adler, J. Colloid Interface Sci. 126 (1) (1987) 314–328.
[19] M. Mahe, M. Vignes-Adler, P.M. Adler, J. Colloid Interface Sci. 126 (1) (1988) 329–336.
[20] V.G. Babak, Colloids Surf. A 85 (1994) 279–294.
[21] K.P. Galvin, A. Cork, T.F. Wall, Colloids Surf. A 113 (1996) 107–116.
[22] P.G. de Gennes, Physica A 249 (1998) 196–205.
[23] A. Mate, O. Masbernat, C. Gourdon, Chem. Eng. Sci. 55 (2000) 2073–2088.
[24] D.M. Eckmann, D.P. Cavanagh, A.B. Branger, J. Colloid Interface Sci. 242 (2001) 386–394.
[25] A.M. Freitas, M.M. Sharma, J. Colloid Interface Sci. 233 (2001) 73–82.
[26] D. Bonn, Curr. Opin. Colloid Interface Sci. 6 (2001) 22–27.
[27] D. Bonn, D. Ross, E. Bertrand, K. Ragil, N. Shahidzadeh, D. Broseta, J. Meunier, Physica A (2002) 279–286.
[28] A. Milchev, A. Milchev, K. Binder, Comput. Phys. Commun. 146 (2002) 38–53.
[29] Y.I. Rabinovich, J.J. Adher, M.S. Esayanur, A. Ata, R.K. Singh, B.M. Moudgil, Adv. Colloid Interface Sci. 96 (2002) 213–230.
[30] C. Peter, J. Wayner, Colloids Surf. A 206 (2002) 157–165.
[31] Y.-T. Tseng, F.-G. Tseng, Y.-F. Chen, C.-C. Chieng, Sensors Actuators A 114 (2004) 292–301.
[32] N. Alleborn, H. Rasziller, Chem. Eng. Sci. 59 (2004) 2071–2088.
[33] A.H. Ibrahim, R.M. Brach, P.F. Dunn, Aerosol Sci. 35 (2004) 1189–1204.
[34] B.D. Nichols, C.W. Hirt, J. Comput. Phys. 12 (1973) 234–246.
[35] O. Ubbink, R. Issa, J. Comput. Phys. 1 (1999) 26–50.
[36] A. Theodorakakos, G. Bergeles, Int. J. Numer. Methods Fluids 45 (2004) 421–443.
[37] M.C. Rhie, L.W. Chow, AIAA-82-0998, 1982.
[38] S.V. Patankar, B.D. Spalding, Int. J. Heat Mass Transfer 15 (1972) 1787–1806.
[39] G. Papadakis, G. Bergeles, Int. J. Numer. Methods Heat Fluid Flow 5 (1995) 49–62.
[40] V.P. Carey, Liquid–Vapour Phase-Change Phenomena, Taylor & Francis, 1992.